

Sodium lidar–observed strong inertia-gravity wave activities in the mesopause region over Fort Collins, Colorado (41°N, 105°W)

Tao Li,¹ C.-Y. She,² Han-Li Liu,³ Thierry Leblanc,¹ and I. Stuart McDermid¹

Received 21 March 2007; revised 16 July 2007; accepted 20 August 2007; published 24 November 2007.

[1] In December 2004, the Colorado State University sodium lidar system at Fort Collins, Colorado (41°N, 105°W), conducted an ~80-hour continuous campaign for the simultaneous observations of mesopause region sodium density, temperature, and zonal and meridional winds. This data set reveals the significant inertia-gravity wave activities with a period of ~18 hours, which are strong in both wind components since UT day 338 (second day of the campaign), and weak in temperature and sodium density. The considerable variability of wave activities was observed with both wind amplitudes growing up to ~40 m/s at 95–100 km in day 339 and then decreasing dramatically in day 340. We also found that the sodium density wave perturbation is correlated in phase with temperature perturbation below 90 km, and ~180° out of phase above. Applying the linear wave theory, we estimated the wave horizontal propagation direction, horizontal wavelength, and apparent horizontal phase speed to be ~25° south of west, ~1800 ± 150 km, and ~28 ± 2 m/s, respectively. The vertical profiles of wave intrinsic period, intrinsic phase speed, and vertical wavelength were also estimated. While the onset of enhanced inertia-gravity wave amplitude in the night of 338 was observed to be in coincidence with short-period gravity wave breaking via convective instability, the decrease of inertia-gravity wave amplitude after noon of day 339 was also observed to coincide with the development of atmospheric dynamical instability layers with downward phase progression clearly correlated with the 18-hour inertia-gravity wave, suggesting likely breaking of this inertia-gravity wave via dynamical (shear) instability.

Citation: Li, T., C.-Y. She, H.-L. Liu, T. Leblanc, and I. S. McDermid (2007), Sodium lidar–observed strong inertia-gravity wave activities in the mesopause region over Fort Collins, Colorado (41°N, 105°W), *J. Geophys. Res.*, *112*, D22104, doi:10.1029/2007JD008681.

1. Introduction

[2] Atmospheric gravity waves (AGW) play an important role in the atmospheric general circulation, structure, variability as well as energy and momentum budgets in the middle and upper atmosphere [Fritts and Alexander, 2003]. Inertia-gravity waves (IGWs) influenced by the Coriolis effect due to the Earth rotation are the common features in the geophysical flows. They are often observable in the stratosphere and mesosphere region temperature and wind fields by radar and lidar [Sato and Yamada, 1994; Riggin *et al.*, 1997; Williams *et al.*, 2004; Nastrom and Eaton, 2006], radiosonde [Tsuda *et al.*, 1994; Yamamori and Sato, 2006], and rocket sounding [Eckermann, 1995; Fritts *et al.*, 1997]. The intrinsic periods of these waves are close to the inertia period ($2\pi/f$, where f is the Coriolis parameter). Also, their

vertical wavelengths typically range from 2–10 km in the lower stratosphere to 5–20 km in the upper stratosphere and mesosphere [Fritts *et al.*, 1988; Riggin *et al.*, 1995]. The earlier observations [Muraoka *et al.*, 1994; Riggin *et al.*, 1995; Sato *et al.*, 1997; Yamamori and Sato, 2006; Nastrom and Eaton, 2006] suggest that the horizontal wavelengths of inertia-gravity waves could be thousands of kilometers, and much longer than those of short-period gravity waves commonly seen by OH all-sky imagers in the mesopause region [Hecht *et al.*, 1987; She *et al.*, 2004a; Li *et al.*, 2005].

[3] Most observations and investigations of inertia-gravity waves relied on wind fields in the lower stratosphere and mesosphere [Tsuda *et al.*, 1994; Muraoka *et al.*, 1994; Riggin *et al.*, 1995; Sato *et al.*, 1997; Nastrom and Eaton, 2006]. Among the rare investigations of inertia-gravity waves in the mesopause region is the temperature and wind study by Hu *et al.* [2002], using the University of Illinois sodium lidar data taken at the Starfire Optical Range, NM. Unfortunately, they did not have daytime coverage and hence there were neither background information nor the temporal variation of the IGW activities. Although they have used the hodograph technique on nighttime data to study the wave characteristics, the obtained wave parameters may vary dramatically when the background wind shear is encountered [Hines, 1989;

¹Table Mountain Facility, Jet Propulsion Laboratory, California Institute of Technology, Wrightwood, California, USA.

²Department of Physics, Colorado State University, Fort Collins, Colorado, USA.

³High Altitude Observatory, National Center for Atmospheric Research, Boulder, Colorado, USA.

Sato and Yamada, 1994]. The Colorado State University (CSU) sodium lidar system located in Fort Collins, CO (40.6°N, 105°W), one of the most robust ground-based lidar systems, is capable of simultaneously observing temperature and horizontal wind as well as sodium density in the mesopause region on a 24-hour weather permitting basis [*She et al.*, 2003, 2004b]. The data from CSU sodium lidar multiple-day continuous observations are especially valuable for the study of the inertia-gravity waves and their dynamical variability in the mesopause region.

[4] In this paper, we will present the strong 18-hour inertia-gravity wave activities observed in mesopause region by the CSU sodium lidar system during ~80-hour continuous campaign in December 2004. The sodium lidar-observed temperature, sodium density, zonal wind, and meridional wind will be presented in section 2, followed by initial analysis of the wave spectra, the temporal evolution of wave perturbations, and the linear least squares fitted amplitudes and phases in section 3. In section 4 we describe the characteristics of this 18-hour inertia-gravity wave derived from the observation according to the linear wave theory. Finally, the discussion and conclusion are presented in sections 5 and 6, respectively.

2. Sodium Lidar Observation

[5] The Colorado State University sodium lidar system was first deployed in 1989 with a two-frequency and one-beam design for the observations of temperature and sodium density in the mesopause region [*She et al.*, 1990]. After a decade of operation in this mode [*She et al.*, 2000], it was upgraded to a three-frequency, two-beam system that enables the observations of temperature, zonal wind, meridional wind and sodium density on 24-hour continuous basis, weather permitting. During the campaign in December 2004, the system receiver employed two 14-inch Celestron telescopes pointing eastward and northward, both at 30° from zenith. The lidar transmitter directed two laser beams into the atmosphere; each aligned parallel to one telescope with ~0.5 m from its axis. In comparison to other lidar systems, the CSU sodium lidar system had a modest power-aperture product of 0.05 Wm². However, owing to the resonance enhancement in laser induced fluorescence, the received signal is sufficient to probe atmospheric instabilities, as well as various atmospheric waves and their mutual interactions [*She et al.*, 2004a; *Li et al.*, 2005]. The signals received by each telescope are binned in 150-m-range bins and integrated for 2 min then stored as raw photon count profiles. Depending on the signal-to-noise ratio of the data and the nature of application, the analysis programs further average the raw photon profiles over a longer time interval and over a larger vertical range. The precision of the measurements for temperature and wind with a 2-km vertical resolution and 1-hour temporal resolution is estimated to be 0.5 K and 1.5 m/s, respectively, at 92 km (sodium peak), and 5 K and 15 m/s, respectively, at both 81 km and 105 km (sodium layer edges), under nighttime clear sky conditions. For the daytime measurement, the Faraday filter is used in the receiver channels to efficiently reduce background by a factor of 6000–8000, which also in turn reduces signal by a factor of 4–5 [*Chen et al.*, 1996]. Therefore the uncertainty of the daytime measurements

increases by at least a factor of ~2.5 more in comparison to the nighttime measurements. The stability achieved by the recently upgraded Faraday filter makes the CSU sodium lidar a unique system for multiple-day campaigns, and enables the study of atmospheric tidal oscillations and planetary waves as well as gravity waves in both temperature and horizontal wind fields [*She et al.*, 2004a, 2004b; *Li et al.*, 2005, 2007a, 2007b].

[6] During an ~80-hour lidar campaign in December 2004, we observed a significant gravity wave breaking event on the night of 3 December 2004 (~0900 UT in day 338). The associated breaking gravity wave was determined to have a short period of 1.5 hours, and its characteristics and background conditions were studied in details by the linear wave saturation theory [*Li et al.*, 2007b]. After this short-period gravity wave breaking event, we observed a significant wave activity with an apparent period of ~18 hours. Since the background wind was determined to be eastward, the intrinsic period of the wave could be longer (if propagating eastward) or shorter (propagating westward) than 18 hours. However, the hodograph analysis indicates that the 18-hour wave propagated to ~25° south of west, leading to the shorter intrinsic period than 18 hours, and hence further suggests that this 18-hour wave is most likely an inertia-gravity wave. To facilitate the study of this observed long-period inertia-gravity wave, we form the hourly mean vertical profiles for all four fields with the vertical resolution of 2 km (4 km) for nighttime (daytime). Shown in Figure 1 are the contour plots of temperature (Figure 1a), sodium density (Figure 1b), zonal wind (Figure 1c), and meridional wind (Figure 1d) during this lidar campaign. Please note that the scales are different for the different variables, and the white colors above 100 km in all four contours represent the removed data due to excessive noise. The semidiurnal oscillation is clearly seen above 95 km in temperature and both wind contours with large amplitude of 15–20 K in temperature, 30–40 m/s in both winds. A significant temperature warming event below 95 km was observed on the night of day 338, which is most likely due to significant downward heat flux caused by the short-period gravity wave breaking [*Li et al.*, 2007b]. Also clearly present in both wind contours, though not clear in either temperature or sodium density, is a long-period wave with downward phase progression starting in the nighttime of day 338, nearly coincident with the short-period gravity wave breaking event, when we also observed a slight increase of peak sodium density near 90 km. In addition, we note that the zonal wind was very strong as large as ~120 m/s near 85–90 km in the daytime of day 339, and that the peak of sodium density near 90 km in the beginning of the campaign decreases gradually to almost a factor of 2 lower at the end of campaign. We do not have a good explanation for these observations.

3. Analysis Results

[7] To extract the dominant wave period information from the data set, we perform spectral analysis on the time series of the vertical profiles of all four fields by using Lomb-Scargle method, which can handle unevenly sampled data [*Lomb*, 1976; *Scargle*, 1982]. Shown in the Figure 2 are the profiles of the normalized Lomb power (the spectral

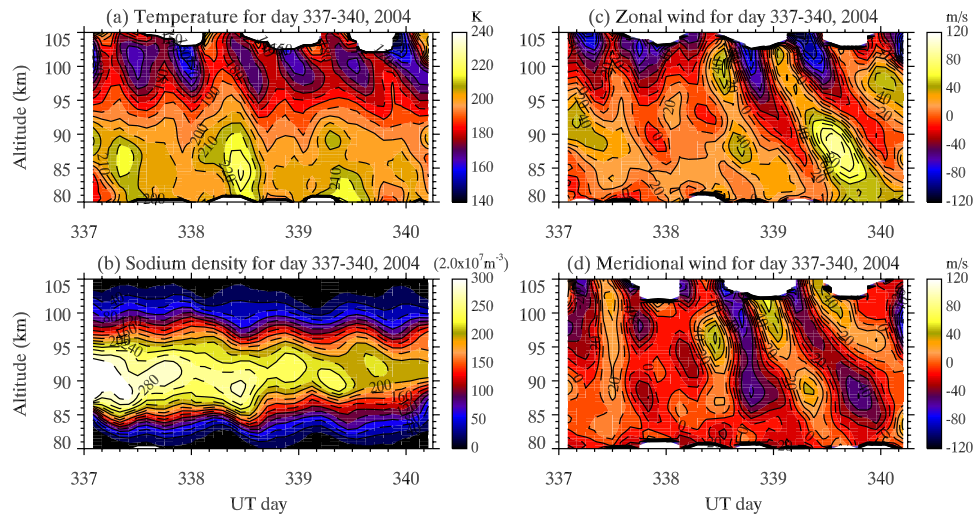


Figure 1. Contour plots of raw (a) temperature, (b) sodium density, (c) zonal wind, and (d) meridional wind for UT day 337–340, 2004, with vertical resolution of 2 km (4 km) for nighttime (daytime), and the temporal resolution of 1 hour. Note that the color scales are different for the contours.

power normalized by variance of the data) of temperature (Figure 2a), sodium density (Figure 2b), zonal wind (Figure 2c), and meridional wind (Figure 2d) as a function of period, with the red and blue stars corresponding to more than 90% and 50% significance respectively. These profiles are presented at 1 km interval, whose vertical scale corresponds to 2 in normalized Lomb power. For the spectrum power lower than 90% significant but more than 50%, we still treat them as viable wave perturbations. The semidiurnal oscillation is clearly present above 95 km in temperature

and zonal wind, above 90 km in meridional wind, and above 100 km in sodium density. Diurnal tide (24-hour period) with significant power in meridional wind and sodium density are observed, respectively, at altitudes below 90 km and below 85 km. In addition, there also exist very strong powers at 18-hour period in zonal wind at most altitudes, meridional wind above 90 km, and moderate temperature and sodium density powers at 95–100 km. Also observable are 26-hour period in both temperature and zonal wind at 85–93 km and sodium density at 85–90 km.

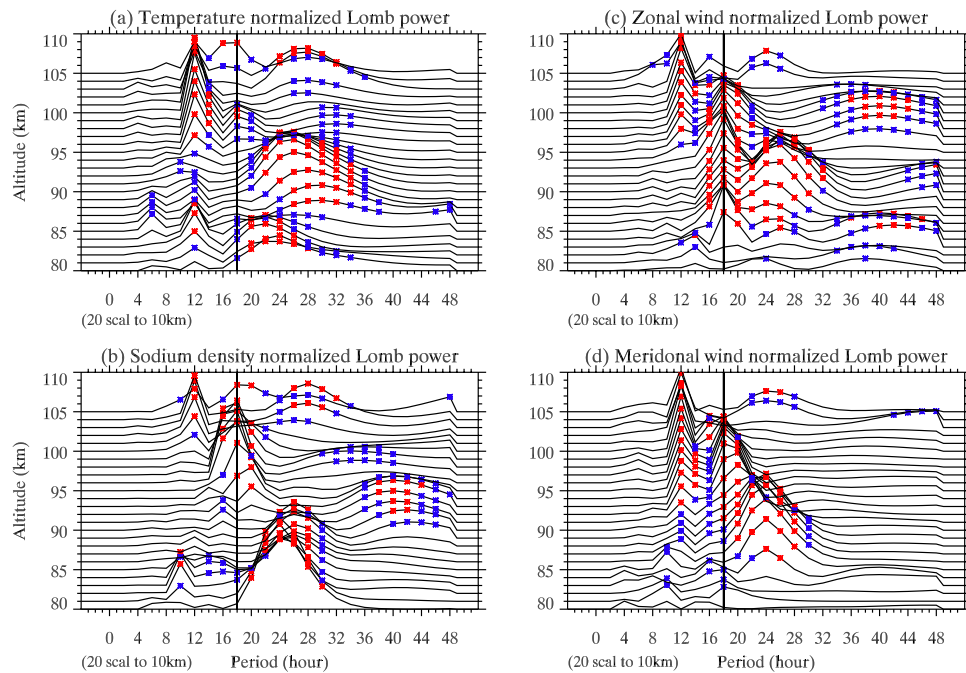


Figure 2. Profiles of the normalized Lomb power of (a) temperature, (b) sodium density, (c) zonal wind, and (d) meridional wind as a function of period, with the red and blue stars corresponding to more than 90% and 50% significance, respectively. These profiles are spaced at 1 km interval, whose vertical scale also corresponds to 2 for the normalized power. The black vertical lines mark the 18 hr period.

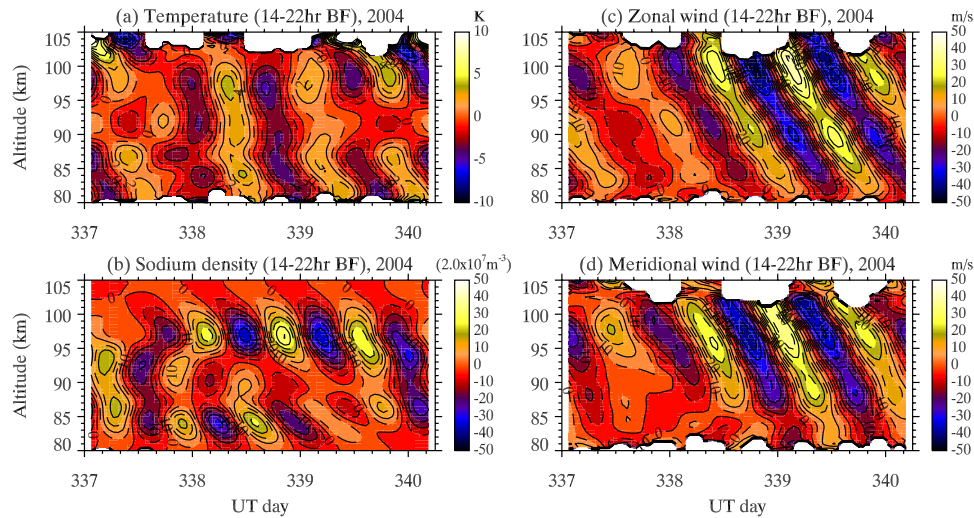


Figure 3. Contours of (a) temperature, (b) sodium density, (c) zonal wind, and (d) meridional wind filtered by a band-pass hamming-window filter with half maxima at periods of 14 and 22 hours.

All these indicate the complexity of wave dynamics during this campaign. The 18-hour period wind perturbations persistent throughout the second half of the campaign with interesting amplitude variability is the main topic of this study.

[8] To extract temporal evolution of the 18-hour inertia-gravity wave, we use the hourly mean profiles with 2 km (4 km) vertical resolution for nighttime (daytime) and first linearly interpolate the minor data gaps (if applied, for this case there is only 2-hour data gaps in the end of day 337 in the meridional wind component) to form an evenly spaced data set, perform FFT transformation on the interpolated data set, and then apply a band-pass hamming-window filter to remove unwanted frequencies and pass perturbations with desired periods, and finally inversely FFT transform back to the time domain. Shown in Figure 3 are the contours of observed temperature (Figure 3a), sodium density (Figure 3b), zonal wind (Figure 3c) and meridional wind (Figure 3d) filtered by a band-pass hamming-window filter with a bandwidth running from 14 to 22 hours (full width half power). The 18-hour wave amplitudes for all four fields were generally weak before day 338, and then increased dramatically when the event of temperature warming below 95 km and horizontal wind acceleration near 100 km was observed in the night of day 338 shown in Figure 1. The strong wind amplitudes could be seen in Figure 3 between 95 and 103 km in day 339 with maxima of ~ 40 m/s near 100 km and 96 km, respectively, in zonal and meridional wind, and then decreased rapidly in day 340, indicating the considerable day-to-day variability of wave amplitudes. Comparing to perturbations in both winds, the temperature and sodium density perturbation is generally weak. Further, the sodium density perturbation is in phase with temperature perturbation below 90 km, and $\sim 180^\circ$ out of phase above 90 km. The weaker amplitude in temperature than those in both wind components is consistent with the gravity wave polarization relation (e.g., equation (2) below) based on the linear wave theory. However, the vertical wavelength in both temperature and sodium density varies with altitude, unlike those in both winds. A possible explanation is that,

since the wave amplitudes in temperature and sodium density are weak, the wave structure could be possibly more sensitive to the broadband noise, and thus variable with altitude.

[9] By using the linear least squares fits on data sets during the time when the wave amplitude was significant (e.g., from 0900 UT of day 338 to the end of campaign), we are able to obtain the 18-hour wave mean amplitudes and phases in temperature, sodium density, and both wind components, shown in Figure 4. The wind amplitudes grow with the altitude and reach as strong as ~ 40 m/s near 101 km in zonal wind and ~ 36 m/s near 96 km in meridional wind respectively. The temperature amplitude is generally around 5 K at most of altitudes except the explosion above 103 km which is most likely due to fitting error. The sodium density amplitudes peaked up at 87 km with a value of $\sim 3.6 \times 10^8 \text{ m}^{-3}$ and 97 km with a value of $\sim 6 \times 10^8 \text{ m}^{-3}$. The maxima and minimum of sodium density amplitudes are corresponding very well with those of temperature amplitudes. The phase plots clearly show downward progression with a speed of ~ 1 km/hr, especially in both winds, indicating the upward wave energy propagation. The meridional wind phase leads the zonal wind phase by ~ 4.5 hours ($\sim 90^\circ$), consistent with the polarization relation (e.g., equation (1) below) of the upward propagating inertia-gravity waves [Fritts and Alexander, 2003]. The sodium density phase is within 1–2 hours difference from temperature phase below 90 km, and ~ 9 -hour ($\sim 180^\circ$) difference above 90 km.

4. Characteristics of the 18-Hour Inertia-Gravity Wave

[10] For the inertia-gravity waves, the horizontal velocity perturbations perpendicular to the direction of horizontal wave propagation, comparing to their high-frequency counterparts, are not zero anymore. By assuming the linear dispersion relation for the inertia-gravity waves, the polarization relation that relates the wave amplitudes of the parallel wind component \hat{u} (in-phase wind, parallel to wave

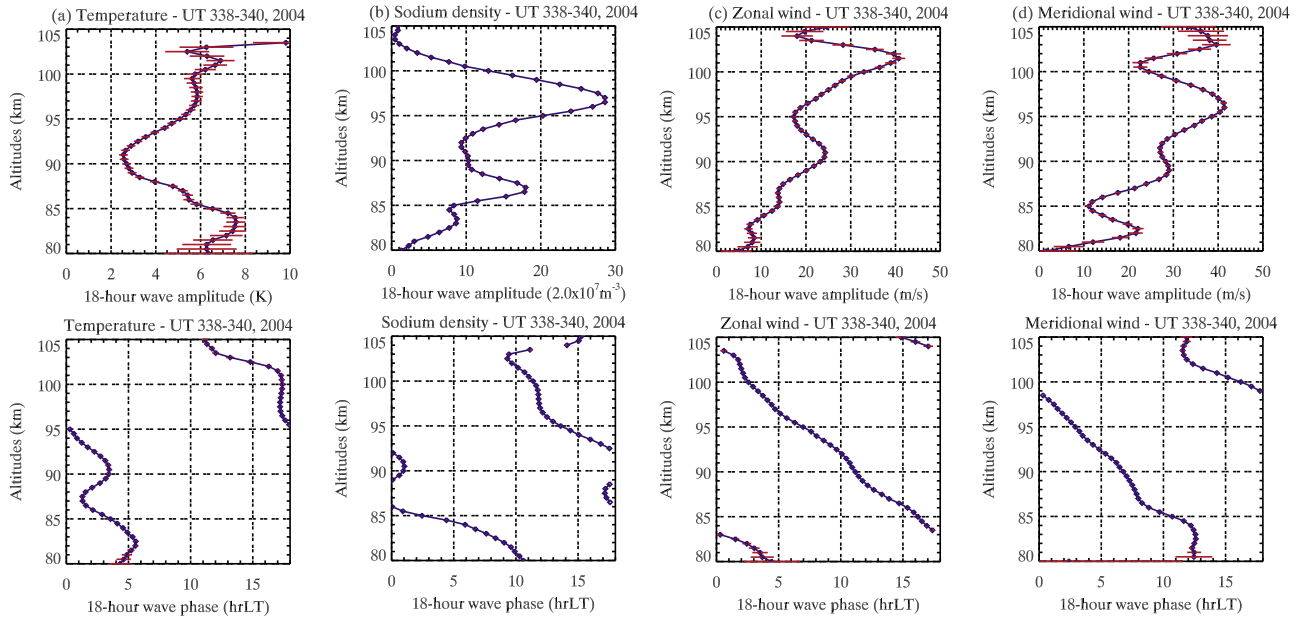


Figure 4. Vertical profiles of (top) 18-hour wave amplitudes and (bottom) phases of (a) temperature, (b) sodium density, (c) zonal wind, and (d) meridional wind obtained by using linear least squares fits on the raw data set between day 338 and 340 when the wave amplitude was significant. The horizontal bars indicate the uncertainty.

propagation direction) with perpendicular wind component \hat{v} (perpendicular to wave propagation direction) is given by [Tsuda *et al.*, 1994; Fritts and Alexander, 2003]

$$\hat{v} = -i \frac{f}{\hat{\omega}} \hat{u}, \quad (1)$$

where f is the Coriolis parameter or inertial frequency; $\hat{\omega}$ is the intrinsic wave frequency. The f at lidar location in Fort Collins, CO is determined to be $\sim 9.465 \times 10^{-5}$ rad/s, corresponding to ~ 18.44 -hour inertia period. On the other hand, the temperature amplitude is also related to in-phase wind amplitude, and given by [Hu *et al.*, 2002]

$$\hat{T} = \frac{H(im + 1/2H)(\hat{\omega}^2 - f^2)}{\hat{\omega}kR} \hat{u}, \quad (2)$$

where H is the scale height; m and k are the vertical and horizontal wave numbers respectively; R is the ideal gas constant. For the upward propagating waves in the Northern Hemisphere ($f > 0$), the \hat{v} leads \hat{u} by 90° , and the hodograph of (\hat{u}, \hat{v}) rotates clockwise with the increased altitude. On the other hand, the hodograph of (\hat{T}, \hat{u}) rotates clockwise with the increased altitude for the wave propagation upward and in the positive in-phase direction ($0^\circ \leq \text{azimuth angle} < 180^\circ$), and counterclockwise with the increased altitude for the wave propagates upward and in the negative in-phase direction [Hu *et al.*, 2002].

[11] Shown in Figure 5 are the hodographs of zonal wind versus meridional wind, and temperature versus in-phase wind at both 0130 UT and 1130 UT in day 339 generated from the band-pass filtered vertical profiles plotted in Figure 3. The reasons why we chose the data in the nighttime of day 339 are that the strong amplitudes in both

zonal and meridional wind were extended to most altitudes at this night and also that the nighttime data have much higher signal-to-noise ratio than the daytime data. The altitude range is chosen from 82 to 103 km, and the increased altitudes are corresponding to the colors from blue to red. The clockwise rotations with increased altitudes in both (u', v') hodographs suggest that the wave energy propagates upward and wave phase progresses downward. The counterclockwise rotations with the increased altitude in the hodographs of temperature versus in-phase wind further imply that the wave propagates horizontally to $\sim 25^\circ$ south of west (the negative in-phase direction). As the gravity wave propagates upward, the amplitude of the wave grows with altitude to compensate the exponential decrease of air density. Hence the idealized hodograph without wave dissipation should present perfect spiral. However, in our case of limited altitude range (~ 20 km) and possible wave dissipation, to estimate the wave propagation direction and intrinsic period, we fitted the hodograph with the ellipse instead of spiral. The perfect ellipse fitting could be seen below 100 km with the major to minor length ratio of ~ 1.85 , corresponding to the intrinsic period of ~ 10 hours (e.g., equation (1)). The estimated intrinsic period from hodograph, however, could be dramatically affected by the background wind shear [Hines, 1989; Sato and Yamada, 1994].

[12] To further estimate the horizontal wavelength and apparent phase speed, we will use the equation derived from the linear dispersion relation of the gravity waves and presented by Liu and Meriwether [2004], i.e.,

$$k = \frac{\omega U}{U^2 - N^2/m^2} \pm \sqrt{\left(\frac{\omega U}{U^2 - N^2/m^2}\right)^2 - \frac{\omega^2 - f^2}{U^2 - N^2/m^2}}, \quad (3)$$

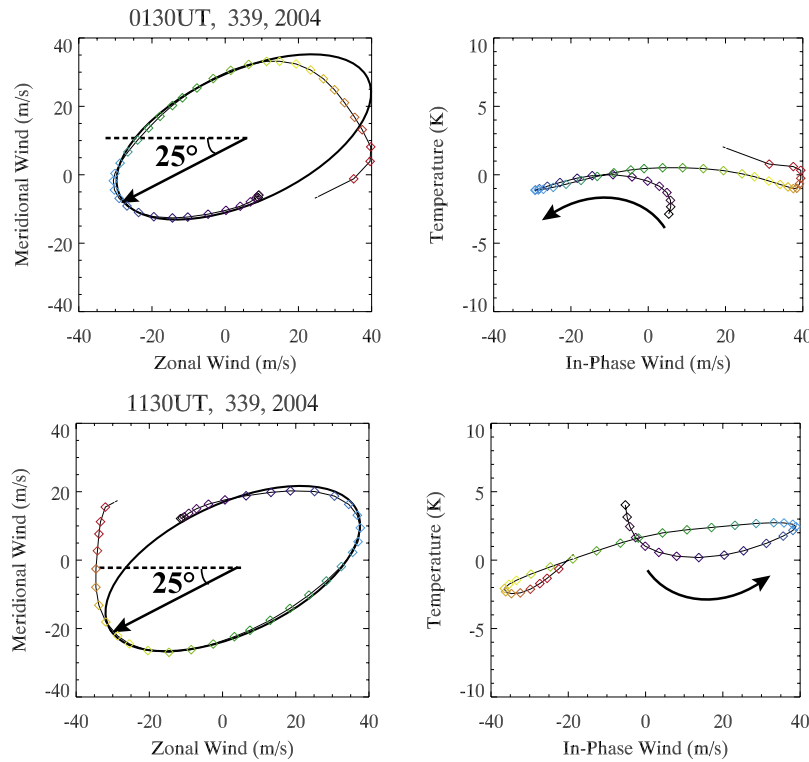


Figure 5. Hodographs of (left) zonal wind versus meridional wind and (right) temperature versus in-phase wind at both (top) 0130 UT and (bottom) 1130 UT in day 339 generated from the band-pass filtered vertical profiles shown in Figure 3. Blue to red color means increased altitudes from 82 km to 103 km. The ellipses are the approximate fitting results.

where ω is the apparent wave frequency; U is the horizontal mean wind projected onto the wave propagation direction; N is the Brunt-Väisälä frequency. The U , N , m , and ω could be obtained from the lidar observations. According to equation (3), the horizontal wavelength, a constant to the ground observer when wave propagates upward, could be estimated from the experimental data. Shown in Figure 6 is the vertical profile of mean wind averaged over the entire campaign and then projected onto the wave propagation direction. There is almost no shear below 89 km, a weak mean wind shear of less than 3 m/s/km between 90 and 97 km, and a relatively stronger mean wind shear of ~ 8 m/s/km above 97 km. It is also clear that the mean horizontal wind changes signs at ~ 102 km from the opposite to the same direction as the horizontal wave vector.

[13] The projected mean wind U in equation (3) is calculated to be $\sim -34 \pm 1$ m/s from Figure 6 by averaging the values in the altitude range (for this case, 82–90 km) where the mean wind shear is as small as possible so that the vertical wavelength is nearly constant. The Brunt-Väisälä frequency N is $\sim 0.019 \pm 0.003$ s $^{-1}$ obtained from mean temperature averaged over the same altitude range as mean wind U . The vertical wavelength is estimated to be ~ 18 km from the zonal wind phase plot below 97 km in Figure 4. The apparent wave period is 18 hours, clearly presented in the spectrum analysis in Figure 2. Following the equation (3) and choosing positive sign, we estimate the horizontal wavelength and apparent phase speed of this 18-hour inertia-gravity wave to be $\sim 1800 \pm 150$ km and $\sim 28 \pm 2$ m/s, respectively. The estimated horizontal wave-

length is in the same scale as the wavelength determined by early radar observations of inertia-gravity waves in the stratosphere and mesosphere [Muraoka *et al.*, 1994; Riggin *et al.*, 1995; Sato *et al.*, 1997]. If we choose the negative sign in the equation (3) for the calculation, the horizontal

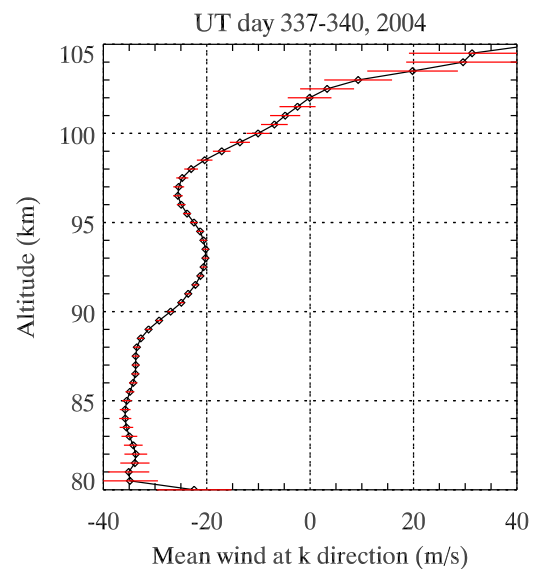


Figure 6. Mean wind vertical profile projected on the horizontal propagation direction of 18-hour inertia-gravity wave. The horizontal bars indicate the uncertainty.

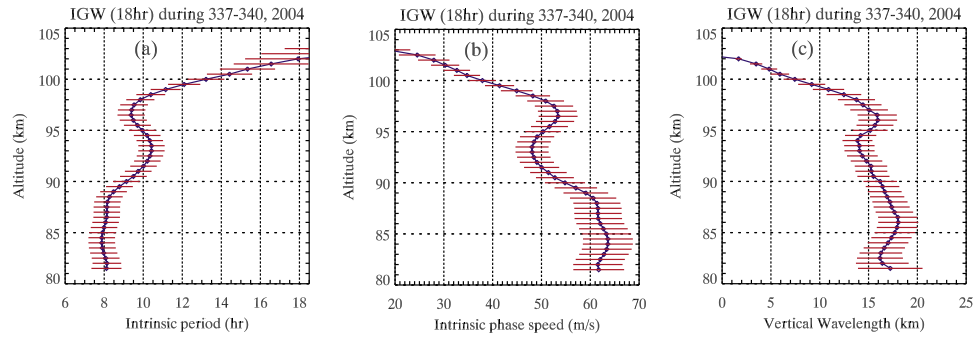


Figure 7. Vertical profiles of (a) wave intrinsic period, (b) intrinsic phase speed, and (c) vertical wavelength. The horizontal bars indicate the uncertainty.

wavelength is obtained to be $\sim 5 \times 10^{10}$ km, which is unreasonable. Therefore we are not going to consider this solution.

[14] Once the horizontal wavelength is determined, we will be able to derive the intrinsic period, intrinsic phase speed, and vertical wavelength, which are all dependent upon the mean wind structure. Shown in Figure 7 are the vertical profiles of wave intrinsic period (Figure 7a), intrinsic phase speed (Figure 7b), and vertical wavelength (Figure 7c) derived from the mean wind profile shown in Figure 6. Above 97 km where the horizontal mean wind shear was large, all three plots show dramatic value changes with the altitude. Below 97 km where the horizontal mean wind shear was small, the wave intrinsic period is between 8–11 hours, consistent with the intrinsic period of ~ 10 hours estimated by using hodograph method in Figure 5. The intrinsic period reaches the inertial period of 18.44 hours at ~ 102 km where the horizontal mean wind was small and positive. Theoretically, at this altitude the vertical wavelength tends to be zero ($m \rightarrow \infty$) and the intrinsic phase is close to the apparent phase speed, indicating that a real critical level is probably located near 102 km. The estimated vertical wavelength is generally around 15–18 km below 97 km, decreases rapidly above 97 km and shrinks to 0 near 102 km.

5. Discussion

[15] According to the dispersion relation of inertia-gravity wave, the ratio of vertical to horizontal group velocity is equal to the ratio of vertical to horizontal wavelength, and is very small [Fritts and Alexander, 2003] (for this case, it is ~ 0.01). Therefore they could be observed in the horizontal direction far away from their sources [Dunkerton, 1984; Eckermann, 1992], often in the lower stratosphere. The 18-hour inertia-gravity wave observed by the CSU sodium lidar in December 2004 was in the mesopause region, which is much higher in altitude than most of other observations of inertia-gravity waves [e.g., Sato and Yamada, 1994; Mitchell et al., 1994; Riggan et al., 1997; Fritts et al., 1997; Nastrom and Eaton, 2006]. Since we do not have much information below the mesopause region, the detailed studies of wave sources are beyond the scope of this paper. However, it may still possibly be excited by the convection in the troposphere, which is one of the most important excitation sources for the inertia-gravity waves [Tsuda et al., 1994; Vincent and Alexander, 2000;

Fritts and Alexander, 2003]. The waves excited by wave sources are usually broadband [Fritts and Alexander, 2003], most of them probably saturate and break down via mean wind filtering process, dissipation, and instability when they propagate upward, and hence are not able to penetrate into mesopause region. Only a small portion of the spectra are able to propagate into higher altitudes. In the winter season of the North Hemisphere, the background zonal winds in both stratosphere and mesosphere are usually eastward [Andrews et al., 1987]. It is possible that this inertia-gravity wave horizontally propagating in the direction of 25° south of west is able to propagate upward into the mesopause region without undergoing significant mean wind filtering, thereby observable by the sodium lidar. Using the estimated wave characteristics shown in section 4, we calculated the vertical and horizontal group velocities below 97 km to be ~ 0.5 km/hr and ~ 50 km/hr, respectively. The estimated vertical group velocity in the mesopause region is much faster than those obtained in the stratosphere [Sato et al., 1997]. This is because the vertical wavelength (wave number) observed in the mesopause region is much longer (smaller) than that observed in the stratosphere (a few kilometers).

[16] The 18-hour wave amplitudes for all four fields were weak before day 338, and then increased dramatically when the event of temperature warming and horizontal wind acceleration was observed at ~ 0900 UT in the night of day 338 (not shown), which is most likely due to a short-period (1.5 hours) gravity wave breaking. This dramatic short-period gravity wave breaking event was studied and discussed in details in the early paper by Li et al. [2007b]. According to the previous model simulations of wave/mean flow interactions [Walterscheid, 1981; Liu and Hagan, 1998], the breaking short-period gravity wave will deposit momentum into the mean flow and induce vertical heat flux, leading to wind acceleration/deceleration and temperature changes around the breaking region. In this case, the breaking 1.5-hour short-period gravity wave in the night of day 338 accelerated the wind toward northeast direction and caused the temperature cooling near 100 km and warming near 97 km [Li et al., 2007b]. As shown in Figure 3, the zonal wind perturbation of 18-hour wave near 100 km is positive at ~ 0900 UT when this 1.5-hour short-period gravity wave saturates and breaks, and thus it could be possibly amplified. Comparing to the perturbation near 100 km one period (18 hours) before, the zonal wind

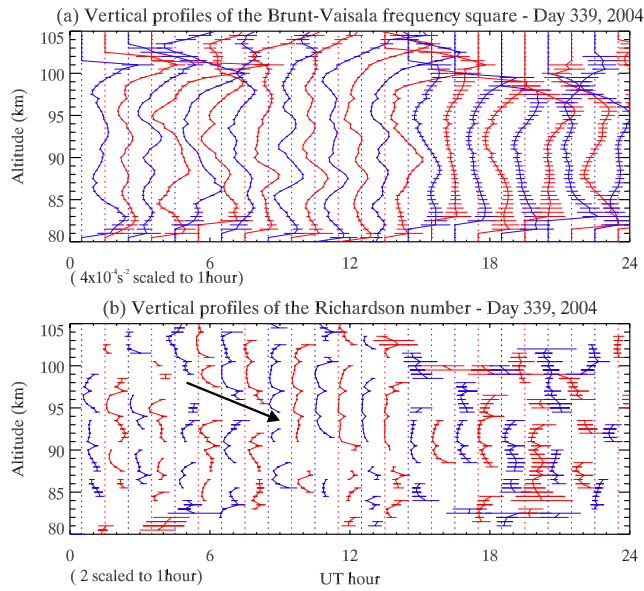


Figure 8. Hourly mean vertical profiles of (a) Brunt-Väisälä frequency square and (b) Richardson number on 4 December (UT day 339) 2004. These profiles are spaced at 1-hour intervals, whose horizontal scale also corresponds to $4 \times 10^{-4} \text{ s}^{-2}$ in Brunt-Väisälä frequency square or 2 in Richardson number. The vertical dotted lines denote the instability threshold corresponding to 0 for Brunt-Väisälä frequency square or 0.25 for Richardson number. Note that in Richardson number plots, the values larger than 2 are ignored. The horizontal bars indicate the uncertainty. The black arrow line indicates the downward progression of instability.

amplitude of 18-hour inertia-gravity wave was increased almost 3 times (from 10 m/s to 30 m/s), after this 1.5-hour short-period gravity wave breaking. At the same time, the temperature perturbation was also amplified near 97 km. Although it is possible that the dramatic increase of the 18-hour inertia-gravity wave amplitude in UT day 338 is just due to its own wave propagation, one more likely explanation is that the breaking of 1.5-hour short-period gravity wave could cause the dramatic amplitude increase of this 18-hour long-period inertia-gravity wave.

[17] We also noticed that the 18-hour wave amplitude in sodium density is positively correlated with the temperature amplitude. However, the sodium density perturbation is in phase with temperature perturbation below 90 km, and $\sim 180^\circ$ out of phase above 90 km. Both the earlier chemical-dynamic model simulation of wave-driven sodium perturbation [Hickey and Plane, 1995] and sodium lidar observation of short-period gravity waves [Bills and Gardner, 1993] implied that, if the chemistry is ignored and only dynamic effects are considered, the sodium density wave perturbation is only dependent on the mean state and temperature perturbation, and independent on all other wave parameters, and the sodium density wave perturbation should be in phase with temperature perturbation below the sodium density peak (~ 90 km) and 180° out of phase above. Our observation of the relation of the 18-hour inertia-gravity wave perturbations in sodium density and temperature is clearly

consistent with this scenario of short-period internal gravity waves.

[18] Further, as shown in Figure 3, the strong amplitudes in both zonal and meridional winds maximized in day 339, and then decreased rapidly in day 340, indicating not only the considerable day-to-day variability of wave amplitudes, but also the possible wave breaking after the wave amplitude reaches its maxima. To explore this possibility of wave breaking, we plot the hourly mean vertical profiles of Brunt-Väisälä frequency square and Richardson number for UT day 339 shown in Figures 8a and 8b, respectively. These profiles are spaced at 1-hour intervals, whose horizontal scale also corresponds to $4 \times 10^{-4} \text{ s}^{-2}$ in Brunt-Väisälä frequency square or 2 in Richardson number. The vertical dotted lines denote the instability threshold corresponding to 0 for Brunt-Väisälä frequency square or 0.25 for Richardson number. In the Richardson number plots, the values larger than 2 are ignored. We clearly see that the atmosphere between 80 and 105 km was convectively stable most of the time in day 339; convective instability was reached at 0430 UT near 103 km and at both 2130 UT and 2230 UT near 100 km, but with the large error bars. However, from the Richardson number plots, we see that within the error bar indicated, there are two layers with the Richardson number equal to or less than 0.25 developed. The lower layer started from the 0030 UT near 95 km and then moved downward until 0630 UT near 90 km; The upper layer started from the higher altitude near 103 km at 0130 UT and then progressed downward with a speed of ~ 1 km/hr (indicated by a black arrow line in the plot), in agreement with the downward phase speed of the 18-hour inertia-gravity wave, and the width of the layer was extended from a couple of kilometers in the beginning to ~ 5 km at 1330 UT. The upper layer is also clearly in phase with the wave maximum peak in the zonal wind component shown in Figure 3c. Meanwhile, we also examined the vertical profiles of the Brunt-Väisälä frequency square and Richardson number for UT day 338 (not shown). Although there was dynamical instability developed between 0930 and 1130 UT near 95–100 km, the atmosphere was stable in most of day, both convectively and dynamically.

[19] It is well known, when the Richardson number reaches 0.25 or less, the atmosphere may be dynamically unstable. As shown in Figure 8, the Richardson number reached ~ 0.25 or less starting near 100 km at ~ 0600 UT in day 339 and progressing downward with a speed of ~ 1 km/hr, comparable to the downward phase speed of 18-hour wave. Although the Richardson number in Figure 8 was calculated from raw data, the observed dynamical instability layers are clearly associated with the 18 hr inertia-gravity wave, further indicating that the 18-hour wave perturbation is the major contributor to dynamic instability. Werne and Fritts [1999, 2001] suggested that the turbulence and mixing could be generated within the inertia-gravity wavefield when the dynamical instability was observed, and then the wind shears and wave amplitudes could be reduced owing to turbulent mixing [Fritts and Alexander, 2003]. Furthermore, the simulation done by LeLong and Dunkerton [1998] indicated that the amplitude threshold required to initiate dynamical instability by inertia-gravity wave is decreased as $\hat{\omega} \rightarrow f$. In the night of 339, the horizontal wind amplitude, intrinsic period, and intrinsic

phase speed at 100 km are determined roughly to be ~ 45 m/s, ~ 14 hours, ~ 40 m/s, respectively. The normalized (by the wave intrinsic phase speed) amplitude threshold for $f/\bar{\omega} = 14 \text{ hours}/18.44 \text{ hours} = 0.76$ without the presence of mean wind shear was predicted by the model to be $a = u'/(c - \bar{u}) = \sim 0.8$. The observed normalized wave amplitude a is ~ 1.1 near 100 km, which is already beyond the theoretical threshold for dynamical instability. On the other hand, the maximum wind shear due to the large wind amplitude near 100 km could be estimated by using the vertical wavelength (~ 8 km near 100 km shown in Figure 7) and horizontal wind wave amplitude (~ 45 m/s near 100 km as shown in Figure 3) and determined to be ~ 35 m/s/km. Although the observed mean wind shear is not too strong near 100 km (~ 8 m/s/km), it is still possible that with the superposition of the wave on the mean state, this inertia-gravity wave could become dynamically unstable and break after the wave amplitude reached its maximum value in day 339.

6. Conclusion

[20] The strong 18-hour inertia-gravity wave activities with considerable variability were observed by the Colorado State University sodium lidar system at Fort Collins, Colorado (41°N , 105°W) during an ~ 80 -hour continuous lidar campaign in December 2004. The wave amplitudes in both winds are getting stronger in day 338 and then peaked in day 339, and finally decreasing rapidly in day 340. The linear least squares fitting on the data set between 338 and 340 shows that the mean amplitudes in both winds are growing with altitude and reach maximum of ~ 40 m/s at 101 km and ~ 36 m/s at 96 km, respectively, for zonal and meridional components, and the temperature amplitudes are generally weak around 5 K at most altitudes. The sodium density perturbation peaks up near 87 km and 97 km with values of $\sim 3 - 6 \times 10^8 \text{ m}^{-3}$. The maxima and minimum of sodium density amplitudes correlate very well with those of temperature amplitudes. As might be expected, the sodium density perturbation is in phase with temperature perturbation below 90 km, and $\sim 180^\circ$ out of phase above 90 km. The downward phase progression in all four fields suggests the upward energy propagation.

[21] According to the linear wave theory, we determined and estimated the characteristics of this 18 hr inertia-gravity wave from experimental data. The wave horizontal propagation direction, horizontal wavelength, and apparent horizontal phase speed are obtained to be $\sim 25^\circ$ south of west, $\sim 1800 \pm 150$ km, and $\sim 28 \pm 2$ m/s, respectively. Since the wave intrinsic period, the intrinsic horizontal phase speed, and the vertical wavelength are all dependent upon the mean wind structure, we estimated the vertical profiles of these parameters based on the mean wind profile obtained by averaging over the entire data set.

[22] In addition, we observed that the atmospheric layers with the dynamics instability in day 339 were clearly associated with the 18-hour inertia-gravity wave. The decrease of the wave amplitude after the noon of day 339 in the filtered contour plots further suggests that the wave breaking due to dynamical instability or shear instability most likely occurred. The strong wind shear induced by the superposition of the inertia-gravity wave with the horizontal

wind amplitude as strong as ~ 45 m/s near 100 km in the daytime of day 339 on the mean wind state could possibly be the trigger of observed dynamical instability. Thus both the onset of enhanced amplitude and decrease of the amplitude of the 18-hour inertial gravity wave were observed to coincide with (possibly triggered by) wave breaking, the former of a short-period gravity wave via convective instability, and the latter of the 18-hour inertia-gravity wave itself via dynamic instability.

[23] In this case study, we addressed temporal variation, wave characteristics, and instability of a strong 18-hour inertia-gravity wave in the mesopause region based on the simultaneous and continuous observations of sodium density, temperature, and horizontal wind for multiple days by the CSU sodium lidar at Fort Collins, Colorado. Because of the need for 24-hour continuous observation of both temperature and wind for this study, it is not achievable before in the mesopause region for the observation of inertia-gravity waves by any other single instrument. This may also be the first time to study the IGW dynamical variability and estimate most of wave characteristics solely from experimental data in the mesopause region. The correlation of temperature and sodium density responses to long-period inertia-gravity wave perturbation is also observed for the first time in the mesopause region. This type of the studies could be further enhanced by using multiple instruments, such as radar and satellite, for simultaneous observations of the wave features below the mesopause region as well as their horizontal features. Further, more cases of inertia-gravity wave activities in the mesopause region should be studied to obtain the seasonal variability of the wave characteristics and their time evolution, and instability. All of these will be beneficial to the model simulations of inertia-gravity waves in this region of the atmosphere.

[24] **Acknowledgments.** The work described in this paper was carried out at the Colorado State University (CSU) and, in part, at the Jet Propulsion Laboratory, California Institute of Technology, under agreements with the National Aeronautics and Space Administration. Additional funding for CSU was provided by grants NAG5-13567 and NNX07AB64G from National Aeronautics and Space Administration, and grant ATM-0545221 from National Science Foundation. H. L. L.'s effort is supported in part by the NASA Sun Earth Connection Theory Program (S-13753-G). The National Center for Atmospheric Research is operated by the University Corporation for Atmospheric Research under the sponsorship of the National Science Foundation.

References

- Andrews, D. G., J. R. Holton, and C. B. Leovy (1987), *Middle Atmosphere Dynamics*, 489 pp., Elsevier, New York.
- Bills, R. E., and C. S. Gardner (1993), Lidar observations of the mesopause region temperature structure at Urbana, *J. Geophys. Res.*, **98**, 1011–1021.
- Chen, H., M. A. White, D. A. Krueger, and C. Y. She (1996), Daytime mesopause temperature measurements using a sodium-vapor dispersive Faraday filter in lidar receiver, *Opt. Lett.*, **21**, 1003–1005.
- Dunkerton, T. J. (1984), Inertia-gravity waves in the stratosphere, *J. Atmos. Sci.*, **41**, 3396–3404.
- Eckermann, S. D. (1992), Ray-tracing simulation of the global propagation of inertia gravity waves through the zonally averaged middle atmosphere, *J. Geophys. Res.*, **97**, 15,849–15,866.
- Eckermann, S. D. (1995), On the observed morphology of gravity wave and equatorial-wave variance in the stratosphere, *J. Atmos. Terr. Phys.*, **57**, 105–134.
- Fritts, D. C., and M. J. Alexander (2003), Gravity wave dynamics and effects in the middle atmosphere, *Rev. Geophys.*, **41**(1), 1003, doi:10.1029/2001RG000106.
- Fritts, D. C., S. A. Smith, B. B. Balsley, and C. R. Philbrick (1988), Evidence of gravity wave saturation and local turbulence production in

- the summer mesosphere and lower thermosphere during the STATE experiment, *J. Geophys. Res.*, **93**, 7015–7025.
- Fritts, D. C., et al. (1997), Equatorial dynamics observed by rocket, radar, and satellite during the CADRE/MALTED campaign: 2. Mean and wave structures, coherence, and variability, *J. Geophys. Res.*, **102**, 26,211–26,216.
- Hecht, J. H., R. L. Walterscheid, G. G. Sivjee, A. B. Christensen, and J. B. Pranke (1987), Observations of wave-driven fluctuations of OH night-glow emission from Sondre Stromfjord, Greenland, *J. Geophys. Res.*, **92**, 6091–6099.
- Hickey, M. P., and J. M. C. Plane (1995), A chemical-dynamic model of wave-driven sodium fluctuations, *Geophys. Res. Lett.*, **22**, 2861–2864.
- Hines, C. O. (1989), Tropopausal mountain waves over Arecibo—A case study, *J. Atmos. Sci.*, **46**, 476–488.
- Hu, X., A. Z. Liu, C. S. Gardner, and G. R. Swenson (2002), Characteristics of quasi-monochromatic gravity waves observed with Na lidar in the mesopause region at Starfire Optical Range, N.M., *Geophys. Res. Lett.*, **29**(24), 2169, doi:10.1029/2002GL014975.
- LeLong, M.-P., and T. J. Dunkerton (1998), Inertia-gravity wave breaking in three dimensions, 1, Convectively stable waves, *J. Atmos. Sci.*, **55**, 2473–2488.
- Li, T., C. Y. She, B. P. Williams, T. Yuan, R. L. Collins, L. M. Kieffaber, and A. W. Peterson (2005), Concurrent OH imager and sodium temperature/wind lidar observation of localized ripples over northern Colorado, *J. Geophys. Res.*, **110**, D13110, doi:10.1029/2004JD004885.
- Li, T., C. Y. She, S. E. Palo, Q. Wu, H.-L. Liu, and M. L. Salby (2007a), Coordinated lidar and TIMED observations of the quasi-two-day wave during August 2002–2004 and possible quasi-biennial oscillation influence, *Adv. Space Res.*, doi:10.1016/j.asr.2007.03.052, in press.
- Li, T., C. Y. She, H.-L. Liu, and M. T. Montgomery (2007b), Evidence of a gravity wave breaking event and the estimation of wave characteristics from sodium lidar observation over Fort Collins, CO (41°N, 105°W), *Geophys. Res. Lett.*, **34**, L05815, doi:10.1029/2006GL028988.
- Liu, H.-L., and M. E. Hagan (1998), Local heating/cooling of the mesosphere due to gravity wave and tidal coupling, *Geophys. Res. Lett.*, **25**, 2941–2944.
- Liu, H.-L., and J. W. Meriwether (2004), Analysis of a temperature inversion event in the lower mesosphere, *J. Geophys. Res.*, **109**, D02S07, doi:10.1029/2002JD003026.
- Lomb, N. R. (1976), Least-squares frequency-analysis of unequally spaced data, *Astrophys. Space Sci.*, **39**, 447–462.
- Mitchell, N. J., L. Thomas, and I. T. Prichard (1994), Gravity waves in the stratosphere and troposphere observed by lidar and MST radar, *J. Atmos. Terr. Phys.*, **56**, 939–947.
- Muraoka, Y., S. Fukao, T. Sugiyama, M. Yamamoto, T. Nakamura, T. Tsuda, and S. Kato (1994), Features of a mesospheric inertia-gravity wave observed with the MU radar, *J. Atmos. Terr. Phys.*, **56**, 1163–1171.
- Nastrom, G. D., and F. D. Eaton (2006), Quasi-monochromatic inertia-gravity waves in the lower stratosphere from MST radar observations, *J. Geophys. Res.*, **111**, D19103, doi:10.1029/2006JD007335.
- Riggin, D. M., D. C. Fritts, C. D. Fawcett, and E. Kudeki (1995), Observations of inertia-gravity wave motions in the stratosphere over Jicamarca, Peru, *Geophys. Res. Lett.*, **22**, 3239–3242.
- Riggin, D. M., D. C. Fritts, C. D. Fawcett, E. Kudeki, and M. H. Hitchman (1997), Radar observations of gravity waves over Jicamarca, Peru during the CADRE campaign, *J. Geophys. Res.*, **102**, 26,263–26,281.
- Sato, K., and M. Yamada (1994), Vertical structure of atmospheric gravity waves revealed by the wavelet analysis, *J. Geophys. Res.*, **99**, 20,623–20,631.
- Sato, K., D. J. O'Sullivan, and T. J. Dunkerton (1997), Low-frequency inertia-gravity waves in the stratosphere revealed by three-week continuous observation with the MU radar, *Geophys. Res. Lett.*, **24**, 1739–1742.
- Scargle, J. D. (1982), Studies in astronomical time-series analysis. 2. Statistical aspects of spectral-analysis of unevenly spaced data, *Astrophys. J.*, **263**, 835–853.
- She, C. Y., H. Latifi, J. R. Yu, R. J. Alvarez II, R. E. Bills, and C. S. Gardner (1990), Two-frequency lidar technique for mesospheric Na temperature measurements, *Geophys. Res. Lett.*, **17**, 929–932.
- She, C. Y., S. S. Chen, Z. L. Hu, J. Sherman, J. D. Vance, V. Vasoli, M. A. White, J. R. Yu, and D. A. Krueger (2000), Eight-year climatology of nocturnal temperature and sodium density in the mesopause region (80 to 105 km) over Fort Collins, CO (41°N, 105°W), *Geophys. Res. Lett.*, **27**, 3289–3292.
- She, C. Y., J. Sherman, T. Yuan, B. P. Williams, K. Arnold, T. D. Kawahara, T. Li, L. Xu, J. D. Vance, and D. A. Krueger (2003), The first 80-hour continuous lidar campaign for simultaneous observation of mesopause region temperature and wind, *Geophys. Res. Lett.*, **30**(6), 1319, doi:10.1029/2002GL016412.
- She, C. Y., T. Li, B. P. Williams, T. Yuan, and R. H. Picard (2004a), Concurrent OH imager and sodium temperature/wind lidar observation of a mesopause region undular bore event over Fort Collins/Platteville, CO, *J. Geophys. Res.*, **109**, D22107, doi:10.1029/2004JD004742.
- She, C. Y., et al. (2004b), Tidal perturbations and variability in mesopause region over Fort Collins, CO (41N, 105W): Continuous multi-day temperature and wind lidar observations, *Geophys. Res. Lett.*, **31**, L24111, doi:10.1029/2004GL021165.
- Tsuda, T., Y. Murayama, H. Wiryosumarto, S. W. B. Harijono, and S. Kato (1994), Radiosonde observations of equatorial atmosphere dynamics over Indonesia: 2. Characteristics of gravity waves, *J. Geophys. Res.*, **99**, 10,507–10,516.
- Vincent, R. A., and M. J. Alexander (2000), Gravity waves in the tropical lower stratosphere: An observational study of seasonal and interannual variability, *J. Geophys. Res.*, **105**, 17,971–17,982.
- Walterscheid, R. L. (1981), Inertia-gravity wave induced accelerations of mean flow having an imposed periodic component: Implications for tidal observations in the meteor region, *J. Geophys. Res.*, **86**, 9698–9706.
- Werne, J., and D. C. Fritts (1999), Stratified shear turbulence: Evolution and statistics, *Geophys. Res. Lett.*, **26**, 439–442.
- Werne, J. A., and D. C. Fritts (2001), Turbulence and mixing in a stratified shear layer: 3D K-H simulations at $Re = 24,000$, *Phys. Chem. Earth*, **26**, 263–268.
- Williams, B. P., D. C. Fritts, L. Wang, C. Y. She, J. D. Vance, F. J. Schmidlin, R. A. Goldberg, A. Mullemann, and F.-J. Lubken (2004), Gravity waves in the Arctic mesosphere during the MaCWAVE/MIDAS summer rocket program, *Geophys. Res. Lett.*, **31**, L24S05, doi:10.1029/2004GL020049.
- Yamamori, M., and K. Sato (2006), Characteristics of inertia gravity waves over the South Pacific as revealed by radiosonde observations, *J. Geophys. Res.*, **111**, D16110, doi:10.1029/2005JD006861.

T. Leblanc, T. Li, and I. S. McDermid, Table Mountain Facility, Jet Propulsion Laboratory, California Institute of Technology, 24490 Table Mountain Road, P.O. Box 367, Wrightwood, CA 92397, USA. (taoli@tmf.jpl.nasa.gov)

H.-L. Liu, High Altitude Observatory, National Center for Atmospheric Research, 3450 Mitchell Lane, Boulder, CO 80307-3000, USA.

C.-Y. She, Department of Physics, Colorado State University, Fort Collins, CO 80523-1875, USA.